Calmodulin Remains Extended upon Binding to Smooth Muscle Caldesmon: A Combined Small-Angle Scattering and Fourier Transform Infrared Spectroscopy Study†

Joanna K. Krueger,‡,§ Stephen C. Gallagher,‡ C.-L. Albert Wang,|| and Jill Trewhella*,‡

Bioscience Division, Mail Stop M888, Los Alamos National Laboratory, Los Alamos, New Mexico 87545, and Boston Biomedical Research Institute, 20 Staniford Street, Boston, Massachusetts 02114

Received November 15, 1999; Revised Manuscript Received January 25, 2000

ABSTRACT: We show that calmodulin (CaM) has an extended conformation in its complexes with sequences from the smooth muscle thin filament protein caldesmon (CaD) by using small-angle X-ray and neutron scattering with contrast variation. The CaD sequences used in these experiments were a C-terminal fragment, 22kCaD, and a smaller peptide sequence within this fragment, MG56C. Each of these sequences contains the CaM-binding sites A and B previously shown to interact with the C- and N-terminal lobes of CaM, respectively [Wang et al. (1997) *Biochemistry 36,* 15026]. By modeling the scattering data, we show that the majority of the MG56C sequence binds to the N-terminal domain of CaM. FTIR data on CaM complexed with 22kCaD or with MG56C peptide show the 22kCaD sequence contains unordered, helix, and extended structures, and that the extended structures reside primarily in the MG56C portion of the sequence. There are small changes in secondary structure, involving ∼12 residues, induced by CaM binding to CaD. These changes involve a net decrease in extended structures accompanied by an increase in α-helix, and they occur within the CaM and/or in the MG56C sequence.

Caldesmon (CaD) was first isolated as a calmodulin (CaM)-binding protein (*1*) and is now known to be a major component of the thin filaments in smooth muscle and nonmuscle tissues (*2, 3*). Electron microscopy shows the ∼90 kDa CaD forms an elongated structure (∼80 nm) (*4*) with compact N- and C-terminal domains connected by a helical segment of about 150 residues (*5*). CaD is believed to play a role in thin filament stabilization and assembly, and CaM/CaD interactions are thought to be involved in regulation of contraction in these tissues (for a review, see *6*). In vitro studies show that CaD binds to F-actin and inhibits actomyosin ATPase activity (*3, 7*). This inhibition is reversed by Ca^{2+}/CaM binding (*8*−*10*). It is speculated that CaM/CaD regulation of the smooth muscle contraction might be functionally equivalent to the regulation of skeletal muscle contraction by troponin C/troponin I (*3*).

The crystal structure of CaM (*11*), like that of troponin C (*12, 13*), shows a dumbbell-shaped structure with two globular Ca^{2+}-binding domains connected by a solvent-exposed α-helix. For the isolated proteins, the interconnecting helix is flexible in solution (*14*−*16*). Each globular domain contains two helix−loop−helix motifs that bind Ca^{2+}. Similar to troponin C, Ca^{2+} binding to CaM results in a conformational rearrangement that exposes a hydrophobic cleft in each globular lobe. The exposed clefts interact with hydrophobic residues found within the CaM-binding domains of a diverse array of target proteins (reviewed in *17*−*20*).

Many of CaM's targets have a short (∼20 residue) CaM-binding region that forms a compact amphipathic, basic helix. The much-studied model for this type of CaM−target enzyme interaction is that with myosin light chain kinase, MLCK. CaM binds with nanomolar affinity to its recognition sequence in MLCK, either as an isolated peptide (*21*−*24*) or within the intact enzyme (*25, 26*). This binding induces a dramatic conformational collapse as CaM's globular lobes encompass the peptide sequence to form interactions with 2 large hydrophobic residues separated by 12 residues. CaM's interaction with phosphorylase kinase (PhK) is distinct from the MLCK-type interaction in that CaM remains extended upon binding to 2 CaM-binding subdomains, each ∼25 residues, in PhK (*27*). These subdomains bind CaM simultaneously, also with nanomolar affinity. This distinctive interaction may be important in CaM regulation of PhK in which, unlike the case for MLCK, CaM is an integral part of a multisubunit enzyme. Structural and functional similarities between CaM in PhK and troponin C in troponin have

† This work was performed under the auspices of the U.S. Department of Energy under contract to the University of California, and was supported by DOE/OBER Project KP1101010 (J.T.) and National Institutes of Health Projects GM40528 (J.T.) and AR41637 (C.-L.A.W.). Neutron scattering data were obtained using instrumentation supported by the NSF under Agreement DMR-9423101 at the Cold Neutron Research Facility at the National Institute of Standards Technology. X-ray scattering data were obtained at the Stanford Synchrotron Research Laboratory using instrumentation supported by the DOE (Basic Energy Sciences and Office of Health and Environmental Research) and the NIH Biomedical Resource Technology Program, Division of Research Resources.

* Correspondence should be addressed to this author. Phone: 505-667-2690. FAX: 505-667-2891. Email: jtrewhella@lanl.gov.

‡ Los Alamos National Laboratory.

§ Present address: Department of Chemistry, 9201 University City Blvd., University of North Carolina at Charlotte, Charlotte, NC 28233.

|| Boston Biomedical Research Institute.

10.1021/bi992638x CCC: $19.00
Published on Web 03/18/2000

been pointed out, as well as similarities in the target sequences with which they interact (*27*−*29*).

The CaM-binding region of CaD is distinct from that in MLCK or PhK. It resides within the C-terminus of CaD, and is composed of at least two ∼9-residue sequence segments (residues 658−666, site A, and 687−695, site B, chicken gizzard numbering) separated by ∼20 residues. These sequence segments bind CaM simultaneously with micromolar affinity (*30*−*32*), and site A is proposed to regulate the inhibitory property of CaD (*33*). Fluorescence energy transfer measurements indicate that CaM adopts an extended structure in its complex with CaD (*34*), similar to CaM in PhK and troponin C in troponin.

The unique characteristics of CaM binding to CaD likely reflect its distinctive function in smooth muscle regulation. To gain further insights into the CaM/CaD interaction, we completed small-angle X-ray and neutron scattering experiments on complexes of CaM with both a 19 kDa C-terminal fragment of CaD, 22kCaD (Lys^{579}−Pro^{756}), as well as a smaller 6 kDa peptide, MG56C (Met^{65}−Gly^{713}). These fragments each contain the two CaM-binding sites A and B. Small-angle X-ray scattering provides information on the overall shapes of the complexes, while the neutron scattering with contrast variation on the CaD-derived sequences complexed with deuterated CaM (dCaM) gives structural information on the individual components within the complexes. To complement the shape information derived from the scattering experiments, we used Fourier transform infrared (FTIR) spectroscopy to evaluate secondary structure content and how it changes upon CaM/CaD complex formation.

MATERIALS AND METHODS

Peptide and Protein Preparation. CaM, in deuterated and nondeuterated forms, was prepared as described by Heidorn et al. (*21*). For all of the experiments described, CaM was fully saturated with Ca^{2+}. Lyophilized MG56C peptide was prepared as described by Wang et al. (*33*) with the sequence: MWEKGNVFSSPGGTGTPNKETAGLKVGVSSRINEWLTKTPEGNKSPAPKPSDLRPGC, corresponding to Met^{658}−Gly^{713} in CaD with a Cys residue at the C-terminus. The CaD-binding sites A and B are underlined. The peptide was brought up in buffer containing 25 mM 3-(*N*-morpholino)propanesulfonic acid (MOPS), pH 7.5, 100 mM KCl, 2 mM dithiothreitol (DTT), and 15 mM $CaCl_2$. The recombinant 22kCaD fragment (Lys^{579}−Pro^{756}) was prepared as described by Wang et al. in ref *35*. Concentrations of 22kCaD and of MG56C were determined by absorbance measurements at 280 nm using extinction coefficients $\epsilon^{1mg/mL} = 1.08$ and 1.63, respectively. CaM concentrations were determined using the forward or zero-angle scattering compared to that of a known standard, lysozyme (*36*, *37*), measured in the same sample cell. For X-ray scattering experiments, CaM, 22kCaD, and 1:1 complexes of CaM with MG56C or with 22kCaD were dialyzed against 25 mM MOPS, pH 7.5, 100 mM KCl, 15 mM $CaCl_2$, and 2 mM DTT immediately prior to measurement. For the neutron scattering experiments, the above buffer was prepared with the desired level of D_2O immediately prior to dialysis, and samples were extensively dialyzed. Samples of the MG56C/CaM and the 22kCaD/CaM complexes were prepared with perdeuterated (100dCaM) and/or partially deuterated CaM in which 62% of the nonexchangeable hydrogen molecules were substituted with deuterium (62dCaM). The deuterated CaM samples were prepared as part of the same batch as those used for the experiments on CaM/MLCK interactions described by Krueger et al. in *25* and *26*. Deuteration levels, therefore, had been determined by NMR spectroscopy and confirmed using neutron contrast variation data.

Scattering Data Analysis and Reduction. Scattering data were reduced to $I(Q)$ versus Q where $Q = 4\pi (\sin \theta)/\lambda$ is the amplitude of the scattering vector, 2θ is the scattering angle, and λ is the wavelength of the X-rays or neutrons. The inverse Fourier transform of the scattering data yields $P(r)$, the probable frequency distribution of interatomic vectors within the scattering particle. $P(r)$ profiles were calculated using the algorithm of Moore (*38*) or GNOM (*39*). $P(r)$ goes to zero at the maximum linear dimension, d_{max}, of the scattering particle, and its zeroth and second moments give the forward scatter, I_0, and radius of gyration, R_g, values, respectively. R_g is defined as the root-mean-square distance of all elemental volumes from the center-of-mass of the particle, weighted by their scattering densities. I_0 is directly proportional to the product of the molar concentration and the square of the molecular weight for particles with the same mean scattering density. Because proteins typically have the same scattering density, I_0 is very sensitive to complex formation and can be used to detect and characterize specific associations or aggregation (*37*). Extraction of structural information on individual proteins or protein complexes in solution from scattering data requires samples that are rigorously free of nonspecific aggregates. I_0 values derived from X-ray scattering data of all samples were compared with those of a standard protein [lysozyme (*36*) or CaM (*37*)] measured in the same sample cell on the same day to ensure the samples were aggregation-free.

When one dimension of a scattering particle is much greater than the other two dimensions, Guinier (*40*) showed that

$$\ln QI(Q) \cong \ln QI_0 - Q^2R_c^2/2 \quad (1)$$

where R_c is the radius of gyration of cross-section and is defined as the root-mean-square distance of all area elements from the center of the cross-sectional area of the particle. A plot of $\log[QI(Q)]$ vs Q^2 thus gives a linear region with a slope that is proportional to R_c. R_c is related to the particle's average cross-sectional radius, R, by

$$R = \sqrt{2}R_c \quad (2)$$

Scattering Data Acquisition. X-ray scattering data were collected using beam line 4-2 at the Stanford Synchrotron Radiation Line (SSRL) (*41*), as well as the X-ray instruments at Los Alamos described by Heidorn and Trewhella (*14*) and Gallagher et al. (*42*). Comparison of the synchrotron data with data measured on the same sample preparations at Los Alamos using the much weaker sealed tube source showed radiation damage effects due to the high X-ray intensities at the synchrotron were insignificant. All neutron scattering measurements were performed with the 30-m SANS instrument (NG3) at the National Institute of Standards and Technology (NIST) (*43*) as described by Olah et al. (*44*). Neutrons with a mean wavelength of 5.0 Å were used with a full width-at-half-maximum (fwhm) of 34%. For the

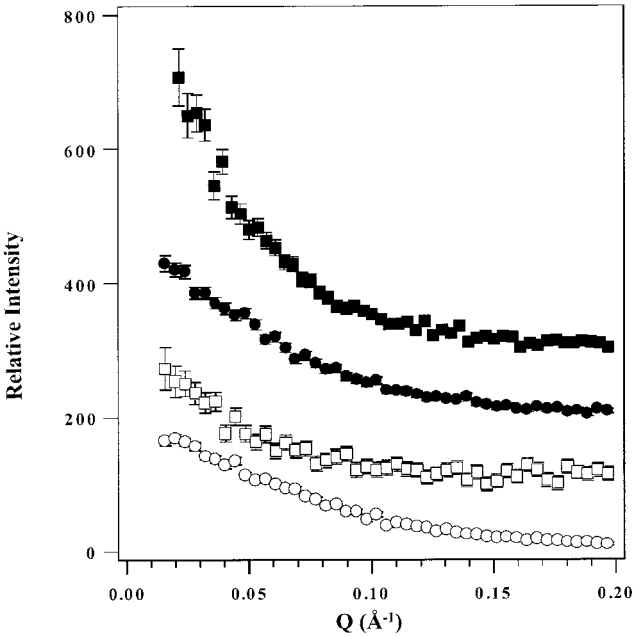

FIGURE 1: X-ray scattering data [*I(Q)* versus *Q*] measured for CaM (○) and the 1:1 complex of MG56C/CaM (●) and 22kCaD (□) and the 1:1 complex of 22kCaD/CaM (■). All samples with CaM were calcium saturated. Scattering data have been offset on the vertical axis for ease of viewing.

contrast variation experiment on the MG56C/62dCaM complex, samples in 0, 20, 40, and 100% D_2O were measured using sample-to-detector distances of 7 and 1.5 m which gave useful data in the *Q*-range 0.01−0.37 Å^{-1}. The excellent overlap of the 7 and 1.5 m data in the *Q*-range 0.048−0.077 Å^{-1} was used to scale data sets with the different *Q*-ranges relative to each other. The solvent matching experiment on the MG56C/100dCaM and 22kCaD/100dCaM complexes in 42% D_2O used a sample-to-detector distance of 2 m, providing data in the *Q*-range of 0.024−0.25 Å^{-1}. Sample cells were 1 mm path length quartz cuvettes for 0%, 20%, 40%, and 42% D_2O and a 4 mm path length quartz cuvette for 100% D_2O (since neutron transmissions per unit length are higher for this sample due to its lower H content).

Fourier Transform Infrared Spectroscopy. FTIR spectra were measured using a FTS 40 FTIR spectrometer with 2 cm^{-1} resolution. To maximize the signal-to-noise ratio, 512 scans were co-added and triangularly apodized. Each measurement was repeated using independent sample preparations. The samples were in a solution cell with CaF_2 windows and a 0.05 mm Teflon spacer. To minimize interference by the rotational fine structure bands from trace amounts of water vapor, the optical bench was maintained under constant positive dry N_2 pressure. Spectra were measured after a minimum 15 min purge and ratioed against a buffer spectrum to give the protein absorbance spectrum free of contributions from the buffer and cell. Temperature was controlled at 20 °C. Samples were prepared and dialyzed against a buffer containing 25 mM MOPS, pH 7.5, 100 mM KCl, 20 mM $CaCl_2$, 2 mM DTT in 99.9% D_2O. FTIR spectra were analyzed as described in Trewhella et al. (*45*).

RESULTS AND DISCUSSION

X-ray Scattering. X-ray scattering data (Figure 1) were collected for a series of protein concentrations for 22kCaD and CaM, as well as 1:1 complexes of CaM/MG56C and CaM/22kCaD in the concentration ranges 0.7−2.5, 3−31, 4−21, and 2.4−4.4 mg/mL, respectively. Each of these data sets showed no concentration dependence in R_g or I_0, indicating that there are no interparticle interference effects and there is no concentration-dependent aggregation. Table 1 therefore gives the structural parameters determined for each protein or protein complex at the highest concentration measured where the statistical errors are minimized. The I_0/c values determined for these data indicate that each of the solutions studied contained identical particles with relative molecular weights expected for the respective proteins and complexes in 1:1 ratios. *P*(*r*) profiles calculated from X-ray scattering data on CaM and its complex with the MG56C CaD peptide and on the 22kCaD fragment and its complex with CaM are shown in Figure 2, with the data normalized to molecular weight squared.

Table 1: Structural Parameters for CaM, 22kCaD, and for the CaM/CaD Complexes Determined Using X-ray Scattering Data[a]

sample	R_g (Å)[b]	d_{max} (Å)[b]
CaM	21.6 ± 0.2	70 ± 2
	(21.5 ± 0.06)	(65 ± 3)
MG56C/CaM	25.6 ± 0.3	80 ± 5
	(24.0 ± 0.1)	(80 ± 5)
22kCaD	33.6 ± 0.8	105 ± 10
22kCaD/CaM	32.2 ± 0.5	100 ± 10

[a] Parameters are calculated using *P(r)* analysis of the X-ray scattering data obtained at Los Alamos. For comparison, values determined using data on complexes of 62% deuterated CaM with CaD collected at SSRL and used for the SASHA calculations are in parentheses. [b] Errors in R_g are based on counting statistics alone. Errors in d_{max} are given as the range over which the *P*(*r*) analyses gave equally good solutions.

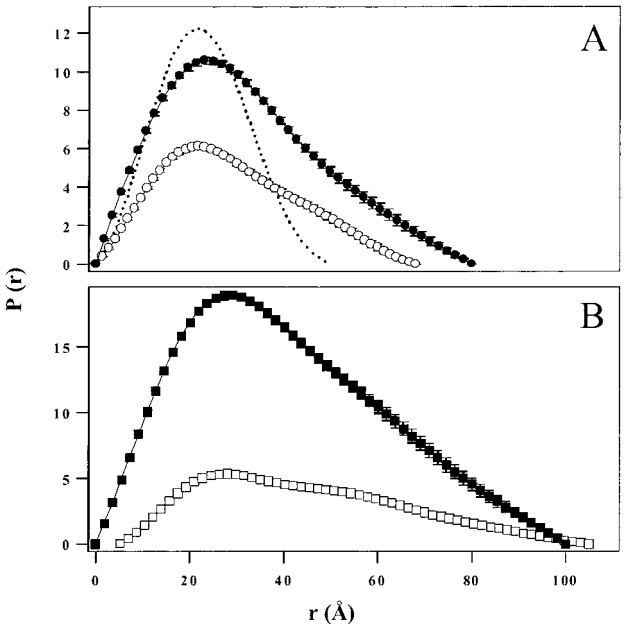

FIGURE 2: *P(r)* functions from X-ray scattering data shown in Figure 1 for (A) CaM (○) and the 1:1 complex of MG56C/CaM (●) and (B) 22kCaD (□) and the 1:1 complex of 22kCaD/CaM (■). For comparison, panel A also shows the *P(r)* profile of the conformationally collapsed CaM as calculated from the NMR solution structure of CaM:MLCK-I (dashed line) (*22*). *P(r)* functions are scaled to the square of the molecular weight.

The CaM/MG56C complex shows an increase in R_g and d_{max} compared with isolated CaM, and the overall shape of the *P(r)* profile for the complex is consistent with CaM

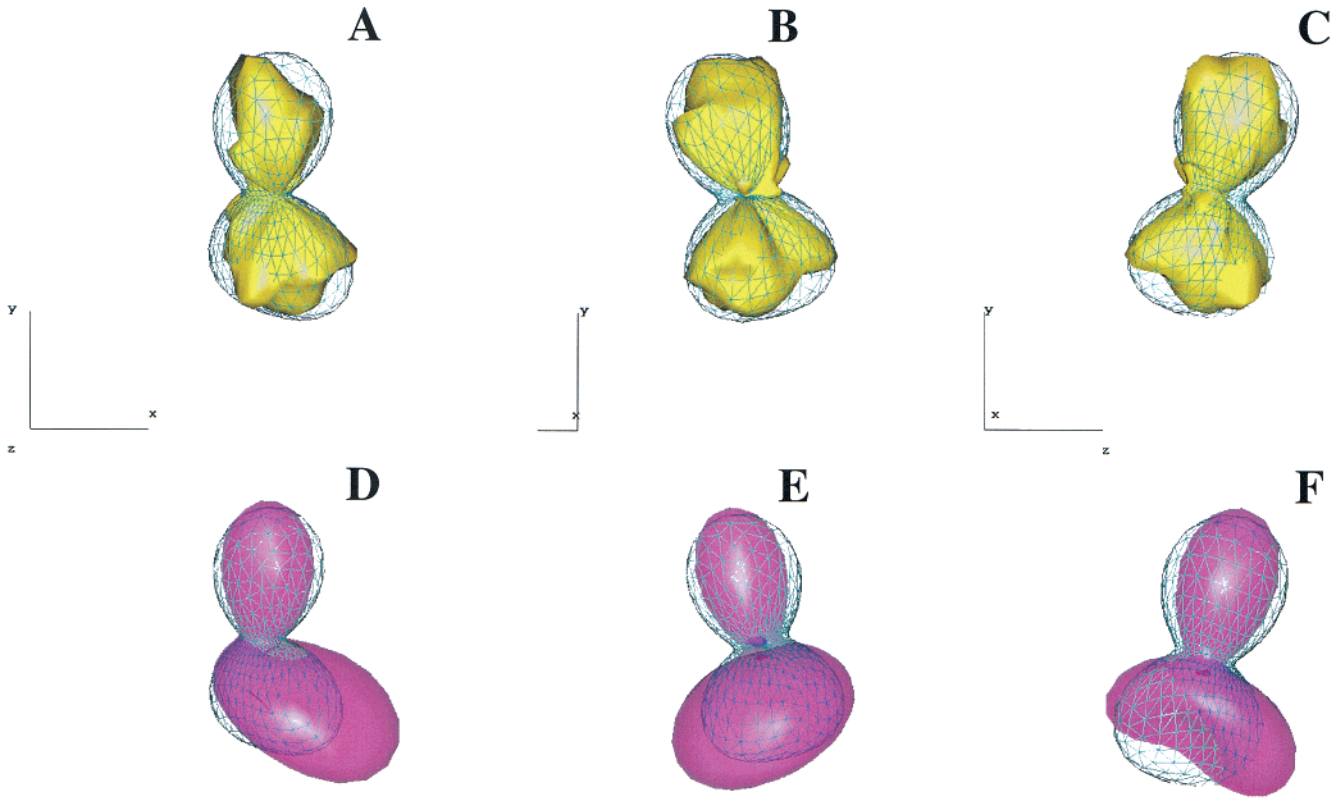

FIGURE 3: Three views of the low-resolution shapes determined using SASHA and small-angle scattering data for (A−C) CaM (light blue frame) overlaid with the envelope shape of CaM determined from the X-ray crystal structure (pdb 3cln) using CRYSOL (solid yellow) and (D−F) for the MG56C/CaM complex (solid magenta) overlaid with the same CaM model in (A−C). The SASHA modeling utilized the scattering data collected at SSRL. The high statistical precision of the SSRL data was required to obtain good model fits.

remaining extended in the complex (Table 1, Figure 2A). For comparison, the $P(r)$ profile of the conformationally collapsed CaM calculated using the NMR structure of CaM bound to MLCK-I peptide is shown in Figure 2A (dotted line) (*22*). To obtain a visual representation of the structural differences between CaM and CaM/MG56C, we used the program SASHA[1] to determine the shape of CaM and the MG56C/CaM complex. SASHA uses spherical harmonics to model solution scattering data and determine the shape of the scattering particle (*46*). It has been used with success on a number of different proteins in solution (*47*). To compare the SASHA output with the crystal structure of CaM, we used the program CRYSOL (*48*) to determine the envelope shape of CaM from its crystal structure (*11*). Figure 3 shows the results obtained using SASHA and CRYSOL. In panels A−C, the CaM envelope determined from the crystal structure is superimposed on the SASHA-derived shape determined using the CaM scattering data. The two-lobed structure of CaM is evident in the shape determination. The exact orientations of the lobes are not perfectly matched between the solution data and the crystal as expected due to the flexibility of the interconnecting helix of CaM in solution (*14*, *15*). The results from SASHA modeling of our MG56C/CaM data are displayed in panels D−F along with the SASHA model determined from the CaM data. This comparison shows that a majority of structural differences between CaM and the MG56C/CaM complex centered on one lobe of CaM.

[1] Program available on www.embl-hamburg.de/ExternalInfo/Research/Sax/index.html.

In an independent modeling approach, CaM was represented as two uniform scattering density ellipsoids to approximate each globular lobe. The volumes and axial ratios of the ellipsoids were varied from 0 to 50 Å in each dimension, and scattering profiles were calculated for 10^4 models using a Monte Carlo simulation program [SASMODEL, described by Zhao et al. in (*49*)]. Best-fit models to the scattering data gave reduced χ^2 values of 1.04, indicating an excellent fit. Comparison of the best-fit models for CaM and CaM/MG56C shows that one lobe was minimally affected by addition of MG56C whereas the other increased significantly in volume. The approximate volumes of each lobe for CaM alone were close to the values expected based on molecular weight (11 000 and 12 000 Å^3 for each lobe, respectively). For the CaM/MG56C complex, the volumes were 13 000 and 20 000 Å^3. Thus, the volume of the second lobe increases by 8000 Å^3, which is close to the value expected for the addition of a 6 kDa MG56C peptide. These results agree well with those obtained using SASHA, indicating that the majority of MG56C sequence is associated with one lobe of CaM.

Site A and site B in the CaD-binding sequence each contain a single Trp residue that interacts with CaM. Intrinsic Trp fluorescence data (*35*) using synthetic peptides based on the CaD sequence, as well as 22kCaD, have shown that site A in the CaD sequence interacts with the C-terminal domain of CaM. The interaction is close to the Ca^{2+}-binding sites (II and IV) and thus deep within the hydrophobic cleft on that domain. Site B, on the other hand, was shown to interact with the N-terminal domain of CaM such that it is more distant from the Ca^{2+}-binding sites (I and II). The

MG56C peptide contains both sites A and B, but site A is minimal with only a single Met N-terminal to the Trp residue that interacts with the C-terminal lobe of CaM. In contrast, site B has 22 residues C-terminal to the Trp residue, and there are 20 residues between the two sites. Based on the fluorescence data, we propose that in our model for MG56C/CaM obtained using SASHA and SASMODEL the smaller lobe corresponds to the C-terminal domain of CaM with the ~7−10 residues of site A tightly associated with the hydrophobic cleft. The larger lobe would correspond to the N-terminal domain of CaM interacting with site B, plus residues N- and C-terminal to site B, some portion of which may be disordered.

The 22kCaD fragment has a highly extended structure for both its free and its CaM-complexed forms as evidenced by the R_g and d_{max} values (Table 1) as well as the overall *P(r)* profiles which are characteristic of rod-shaped particles (Figure 2B). Guinier analysis for rodlike structures (eq 1) of the scattering data from 22kCaD and the 22kCaD/CaM complex gave R_c values of 13.9 ± 0.9 and 13.3 ± 0.5 Å, respectively, with corresponding average cross-sectional radii of ~20 and 19 Å. CaM binding to 22kCaD results in quite small changes in the R_g, R_c, and d_{max} values, indicating the 22kCaD structure remains elongated and rod-shaped. The small decrease in R_g indicates the CaM-binding site is close to the center of mass of the structure. The 22kCaD or the 22kCaD/CaM data could not be modeled using SASHA, due to the highly elongated shape of these particles which makes shape restoration from scattering data difficult.

Neutron Scattering. The intensity of the scattering from a protein in solution depends on its "contrast" with respect to the solvent. This contrast is calculated as the difference in scattering density of the protein from that of the solvent. Because the neutron scattering lengths for hydrogen (^{1}H or H) and deuterium (^{2}H or D) are opposite in sign, substituting H for D can dramatically change the scattering density, either of a protein or of its solvent. If the scattering density of one of the protein components equals that of the solvent (i.e., it has zero contrast), then it is "solvent matched" and contributes nothing to the scattering. A nondeuterated protein with ~42% D_2O is solvent matched. As a result, for a complex of a deuterated protein and a nondeuterated protein in ~42% D_2O, only the deuterated component contributes to the scattering, and thus its shape parameters can be determined. We previously used this type of solvent matching to determine the shape of MLCK with and without substrates bound in a complex with deuterated CaM (*26*). Alternatively, by measuring neutron scattering data for the complex in solvents with a range of D_2O concentrations, one can mathematically extract the scattering profiles for the individual components as described in Krueger et al. (*25*, *26*).

We made complexes of perdeuterated CaM with the 22kCaD fragment and with the MG56C peptide and measured small-angle neutron scattering data for each of them in 42% D_2O. At this contrast, the CaD molecules have a scattering density that is equal to the solvent, and only the deuterated CaM component contributes significantly to the scattering. Using these data, we determined $P(r)$, R_g, and d_{max} values for the 100dCaM within the two CaM/CaD complexes (Table 2). The *P(r)* curve for the 100dCaM/MG56C complex in 42% D_2O is shown (Figure 4) and represents vector lengths from the 100dCaM component within the complex. The corresponding curve derived for the scattering data on the 22kCaD/100dCaM complex is the same, within error, and is not shown for simplicity of the figure. The d_{max} and R_g values (Table 2) determined from the $P(r)$ analyses of CaM in the complexes are larger than those determined for 100dCaM free in solution. The scattering experiments measure the time and ensemble average of the structures present in solution. Free CaM in solution has a flexible interconnecting helix region, and the average distance between the lobes is somewhat closer than in the crystal structure (*11*). In the complex, it appears that the interactions with the CaD sequence hold the lobes in a fixed relationship with respect to each other, or possibly simply restrict the flexibility such that the average separation of the lobes is somewhat greater than for the free CaM in solution. Either way, CaM remains in an extended conformation when it binds to MG56C or the 22kCaD fragment.

A neutron contrast series was also performed on the CaM/MG56C complex in which the solvent deuteration level was systematically varied over the widest range possible. We measured five scattering data sets with different D_2O levels in the solvent (Figure 5) for the MG56C complexed with 62% deuterated CaM. The 62% deuterated CaM was used because it was available and its deuteration level had been determined in a previous neutron scattering experiment (*26*). The 62% deuteration level was also convenient for collecting scattering data either side of the solvent match point for the complex which aids in the analysis. An additional contrast point was obtained from the X-ray scattering data (Figure 1) by scaling it to the neutron scattering data (using eq 24.8 in *50*). We extracted the $P(r)$, R_g, and d_{max} for 62dCaM within

Table 2: Structural Parameters for CaM Bound to CaD Determined from Neutron Scattering Solvent Matching and Contrast Variation Data[a]

	R_g (Å)	d_{max} (Å)
62dCaM (SAXS)	21.4 ± 0.03	68 ± 2
100dCaM (SAXS)	20.8 ± 0.3	68 ± 2
62dCaM in its complex with MG56C (contrast variation)	23.2 ± 0.3	75 ± 5
100dCaM in its complex with MG56C (solvent matching)	23.2 ± 0.3	75 ± 5
100dCaM in its complex with 22kCaD (solvent matching)	22.3 ± 2.2	75 ± 5

[a] X-ray scattering results for the deuterated CaMs are shown for comparison.

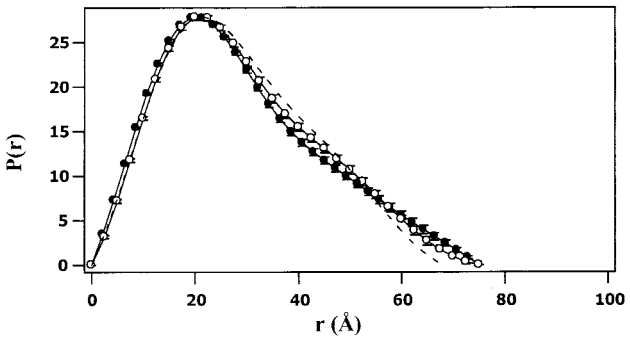

FIGURE 4: *P(r)* functions for CaM within the CaM/MG56C complex determined from the solvent matching experiment (●) and the neutron contrast series (○). For comparison, the *P(r)* profile of isolated CaM is shown as a dashed line. The scattering profile for CaM, $I_{CaM}(Q)$, was extracted from the contrast series data by the method described in Krueger et al. (*25*)

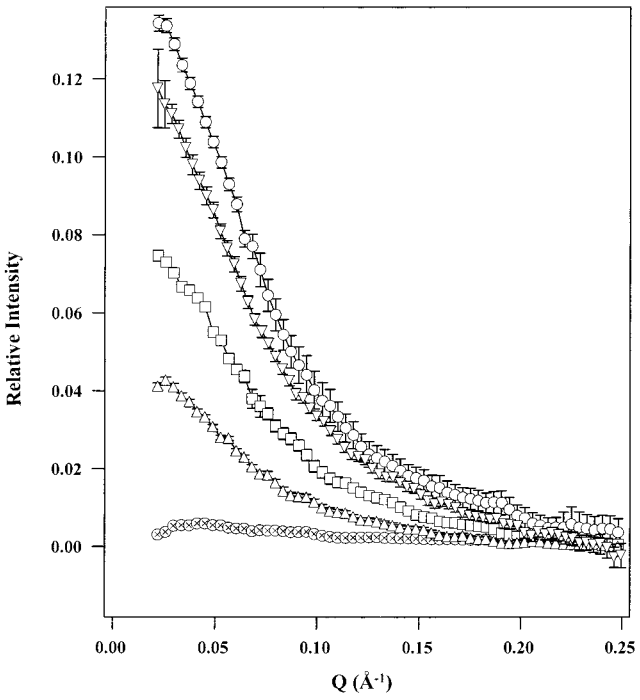

FIGURE 5: Scattering data reduced to *I(Q)* versus *Q* from neutron scattering measurements for 62dCaM/MG56C samples in 0% (○), 20% (□), 40% (△), and 100% (⊗) D_2O and for 100dCaM/MG56C in 42% D_2O (▽). The scaling of the neutron scattering data reflects their relative contrast factors.

the 62dCaM/MG56C complex from the contrast series data as described in Krueger et al. (*25*, *26*). The result is the same within error as obtained for the solvent matching experiment using the 100dCaM (Figure 4, Table 2). The contrast series also provides information on the contrast match point for the complex. Because the deuteration level for the 62dCaM had been determined from previous neutron scattering experiments (*26*), the contrast match point for the complex can be used to confirm that the nondeuterated 22kCaD was solvent matched at 42% D_2O. These two independent neutron scattering experiments thus bring us to the same conclusion, and also support our interpretation of the X-ray scattering data. CaM has an extended conformation in its complexes with the MG56C peptide from CaD.

Fourier Transform Infrared Spectroscopy. Figure 6 shows the buffer-subtracted FTIR absorbance spectra for CaM, MG56C, 22kCaD, and the MG56C/CaM and 22kCaD/CaM complexes, each normalized with respect to protein concentration in milligrams per milliliter for convenient display (for the difference spectra discussed below and shown in the bottom panels of Figure 6, the normalizations were to molar concentration). Bands in the amide I′ region (1620−1700 cm^{-1}) are assigned to the carbonyl stretching frequencies of residues participating in different secondary structure elements within a protein (*51*), while bands in region ∼1540−1600 cm^{-1} are assigned to the carboxylate stretching frequencies of Asp and Glu side chains. To better resolve the components contributing to the amide I′ band, the spectra were Fourier self-deconvolved (Figure 7) using the standard parameters provided by IRPRO software from BIORAD. The frequencies obtained from this deconvolution were used in the global curve-fitting analysis (*52*) to determine the intensities of each band. In this analysis, the frequencies of the bands were kept constant, and the intensities were

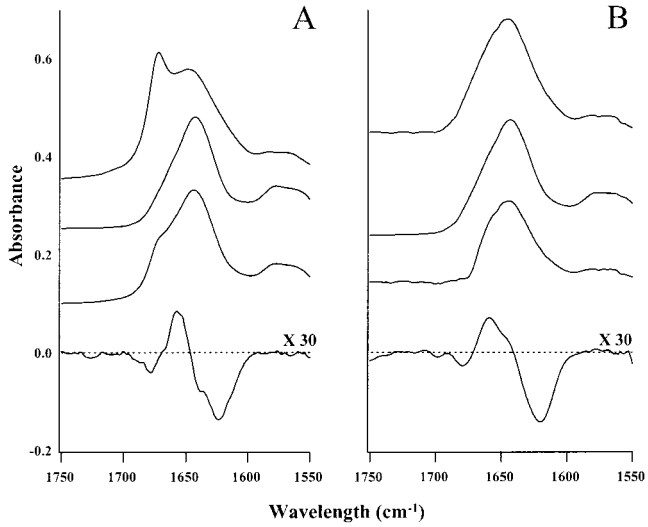

FIGURE 6: From top to bottom: (A) FTIR absorbance spectra for MG56C, CaM, and MG56C/CaM and FTIR difference spectra for MG56C/CaM minus CaM minus MG56C. (B) From top to bottom: FTIR absorbance spectra for 22kCaD and 22kCaD/CaM and FTIR difference spectra for 22kCaD minus MG56C and for 22kCaD/CaM minus CaM minus 22kCaD. The absorbance spectra are scaled to the CaM concentration in milligrams per milliliter for convenient display. The difference spectra were calculated by normalizing the spectra first to molar concentration, and then subtracting (0.26 MG56C + 0.74 CaM) from the MG56C/CaM complex, and (0.53 22kCaD + 0.47 CaM) from the 22kCaD/CaM complex. The difference spectra were then multiplied by 30 for display. All FTIR data were collected using samples with calcium-saturated CaM.

allowed to vary randomly until a perfect fit to the spectrum was obtained as evidenced by a reduced χ^2 of 1.0. This same analysis was used to determine the relative intensities of the resolved bands in the amide I′ region of spectra for CaM, MG56C, 22kCaD, and for the complexes. Because the intensities are proportional to the number of carbonyls contributing to the band, they provide an estimate of the number of residues in each secondary structure type. This analysis was repeated on independent sample preparations, and the results were the same within 1%.

The relative intensities for the bands in the amide I′ region of the spectrum for CaM compare well with those previously determined for the Ca^{2+}-saturated form of the protein (*45*). CaM shows a strong band at 1644 cm^{-1}, previously attributed to a combination of solvated helix plus unordered structure, and a weaker band at the frequency assigned to α-helix (1651 cm^{-1}). There are also bands at 1626, 1633, and 1673 cm^{-1} attributed to extended chain. The bands at 1626 and 1633 cm^{-1} contain contributions from the neighboring bands in the carboxylate stretching frequency region which were accounted for in the global analysis (Table 2, also see below). The bands in the region 1658−1663 cm^{-1} are attributed to turns and bends and were assigned to a common frequency of 1661 cm^{-1} for the global analysis.

The spectrum for the 22kCaD fragment has two approximately equal intensity bands at frequencies assigned to unordered (1641 cm^{-1}) and α-helix structure. There are also smaller contributions from extended chain structures. For MG56C, there are approximately equal proportions of extended chain, helix, and random coil structures. MG56C is approximately one-third (31.5%) the size of 22kCaD. Thus, the extended chain band at 1673 cm^{-1} for MG56C with 32%

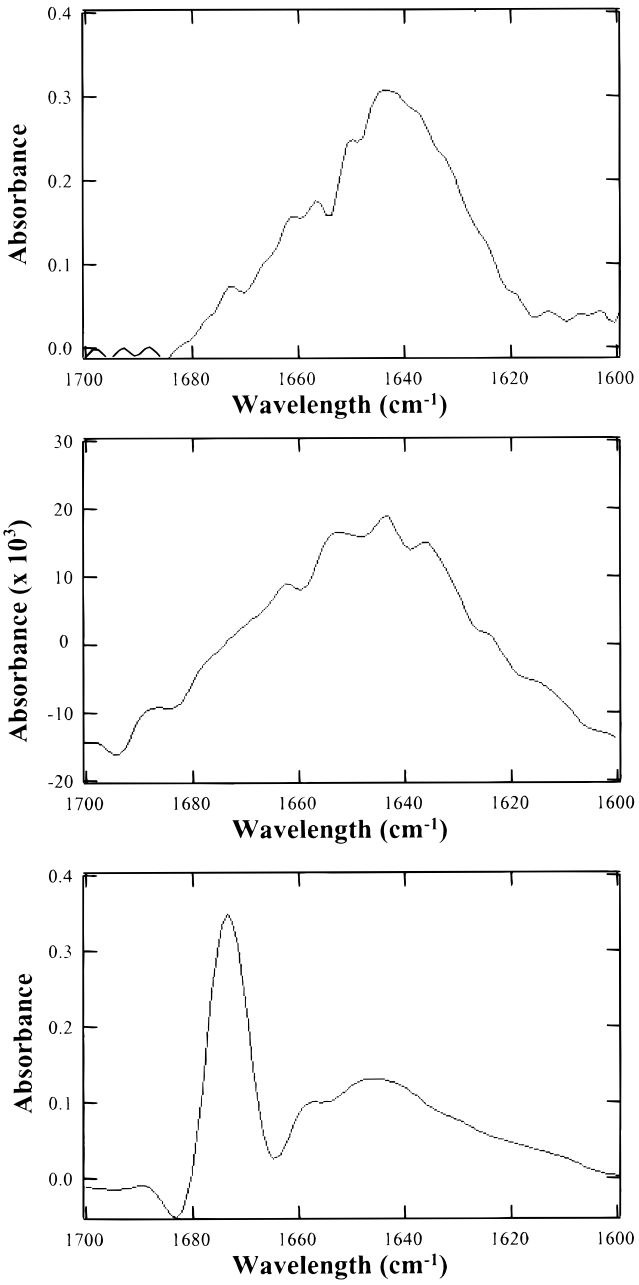

FIGURE 7: Fourier deconvolution of amide I′ bands of the isolated proteins. (A, top) CaM, (B, middle) 22kCaD, and (C, bottom) MG56C.

of the total amide I′ intensity corresponds to an approximately equivalent number of residues involved in extended chain structure as in the 22kCaD fragment which has 10% of the amide I′ intensity in the equivalent band. It appears, therefore, that the extended chain structure is localized in the MG56C sequence, and the remaining structure in 22kCaD is predominantly α-helix and unordered structure.

The bottom spectra in Figure 6 are difference spectra (shown times 30 the intensity) calculated by subtracting the spectra for each of the isolated components from the spectrum for the complex. The component spectra were normalized to molar concentration and subtracted according to their molar ratios. The resulting difference spectra highlight where the changes occur when the CaD sequences bind CaM. They show a net loss of absorbance at 1620 and 1673 cm^{-1} and a net gain of absorbance at 1651 cm^{-1} when

Table 3: Relative Proportions of Secondary Structure Elements for Isolated CaM and CaD Peptides and the Complexes They Form Calculated from the FTIR Spectra[a]

	relative intensity of bands (cm^{-1}) in amide I′ region (% of total)						
	1626	1633	1641	1644	1651	1661	1673
CaM	12.0	18.0	0.0	43.0	11.0	9.0	7.0
22kCaD	3.0	5.0	41.0	0.0	39.0	1.0	11.0
MG56C	2.0	3.0	30.0	0.0	29.0	3.0	32.0
22kCaD/CaM	5.5	11.0	21.0	21.0	29.0	5.5	7.0
22kCaD + CaM	7.5	11.5	20.5	21.5	25.0	5.0	9.0
MG56C/CaM	4.0	12.5	10.5	29.0	26.0	7.5	10.0
MG56C + CaM	9.0	13.0	10.0	30.0	16.0	7.0	15.0

[a] The percentages were determined by global curve-fitting analysis (*52*) and are given as a percentage of the total amide I′ intensity. For comparison, the sum of secondary structures for the isolated components is given below each complex. The sums are scaled to the same ratio as the complexes. Spectra were recorded for independent sample preparations, and the parameters determined for each measurement were the same within 1%.

CaM binds either MG56C or the 22kCaD fragment. Note that because the carboxylate side-chain bands are inherently more intense than the amide I′ bands, the changes in environment experienced by the carboxylates upon complex formation give rise to large changes that overlap with the amide I′ changes at 1620 cm^{-1}. To quantitate the changes and assign them correctly, the global curve-fitting analysis of the spectra for each complex and their components was carried out over the range 1500−1700 cm^{-1} which includes the amide I′ and the side chain carboxylate bands. Table 3 gives the relative intensities in each band in the amide I′ region as a percentage of the total amide I′ intensity. Upon binding of MG56C to CaM, there is an overall loss of intensity associated with extended chain structure (5% each at 1626 and 1673 cm^{-1}) and a gain of intensity associated with helical structure (10% at 1651 cm^{-1}). Similarly, upon binding 22kCaD to CaM, there is a net loss of extended chain structures (2% each at 1626 and 1673 cm^{-1}) and a net gain in helix (4% at 1651 cm^{-1}). The observed changes for 22kCaD involve approximately the same number of residues as seen for the MG56C/CaM complex. It therefore appears that the conformational changes observed for 22kCaD and/or MG56C binding to CaM lie in the MG56C or CaM sequences, or both. The 4% gain in helical structure in the 22kCaD/CaM complex compared to the free components equates to approximately 12 residues. The stabilization of CaM's interconnecting helix could account for part of the change. NMR relaxation studies indicate that 5 residues, 77−81, of CaM are not helical in the isolated solution form of CaM (*15*). In addition, a conversion of extended chain in the CaD sequence is supported by the slight shortening (by ∼5 Å) of 22kCaD observed upon binding CaM. The extended chain is approximately 4 Å per residue, compared to 2 Å per residue for α-helix.

Our FTIR data agree well with the recent NMR data from Zhou et al. (*53*) that show binding of CaM to CaD results in helix forming in CaD (C-terminal half of Arg^{675}−Lys^{695}, which includes only the second CaM-binding site of the MG56C sequence) with smaller changes in CaM. Further, Zhang and Vogel (*54*) show that addition of the helix-promoting solvent TFE to CaD (Gly^{651}−Ser^{667}, which includes only the first CaM-binding site of the MG56C sequence) or addition of CaM results in formation of an

α-helix involving the central 10 residues of this peptide. The combined observations of Zhou et al. (*53*) and Zhang and Vogel (*54*) thus support some α-helix forming within the MG56C sequence upon binding CaM. Zhang and co-workers (*55*) also report evidence that CaD interacts with both lobes of CaM, and that residues in the C-terminal half of the MG56C sequence become α-helical upon binding CaM.

CONCLUSION

The small-angle X-ray scattering and FTIR data on CaM complexed with 22kCaD as well as a smaller MG56C peptide, each of which contains the two putative CaM-binding sites, have provided insights into the nature of the CaM/CaD interaction. The scattering data show that CaM is extended when complexed with MG56C and the 22kCaD fragment, and that the majority of the MG56C sequence is associated with one lobe. The FTIR data indicate the 22kCaD sequence contains unordered, helix, and extended structures, and that the extended structures reside primarily in the MG56C portion of the sequence. There are small changes induced by CaM binding to CaD involving ~12 residues in a loss of extended chain and gain in α-helical structure. These changes occur within CaM, perhaps in the central helix region, and/or in the MG56C sequence.

Scattering data on CaM complexed with its binding domains from PhK (*27*) as well as troponin C complexed with troponin I peptides (*56*) or with intact troponin I (*44*, *57*) show extended structures for CaM and troponin C, respectively, in these complexes. Also similar to troponin C/troponin I, CaM and CaD have been shown to bind in an antiparallel manner (*35*). The extended structure of CaM in complex with CaD, which is markedly different from its collapsed structure in the complex with MLCK enzyme (*25*, *26*), may be needed for a dynamic interaction with CaD. A dynamic CaM/CaD interaction could be key to the reversal of the inhibitory action of CaD in a mechanism similar to the modulation of the action of troponin I by troponin C.

ACKNOWLEDGMENT

We thank Dr. Susan Krueger for assistance in the neutron scattering data acquisition at the National Institute of Standards Technology, and Dr. H. Tsuruta for assistance in X-ray scattering data acquisition at Stanford Synchroton Radiation Laboratory.

REFERENCES

1. Sobue, K., Murimoto, Y., Inui, M., Kanda, K., and Kakiuchi, S. (1982) *Biomed Res. 3*, 188.
2. Furst, D. O., Cross, R. A., De Mey, J., and Small, J. V. (1986) *EMBO J. 5*, 251.
3. Marston, S. B., and Lehman, W. (1985) *Biochem. J. 231*, 517.
4. Marston, S. B., and Huber, P. A. (1996) Caldesmon. in *Biochemistry of Smooth Muscle Contraction* (Barany, M., Ed.) pp 77−90, Academic Press, Inc., San Diego.
5. Wang, C. L. A., Chalovich, J. M., Graceffa, P., Lu, R. C., Mabuchi, K., and Stafford, W. F. (1991) *J. Biol. Chem. 266*, 13958.
6. Mabuchi, K., and Wang, C. L.-A. (1991) *J. Muscle Res. Cell Motil. 12*, 145.
7. Ngai, P. K., and Walsh, M. P. (1984) *J. Biol. Chem. 269*, 3656.
8. Smith, C. W., Pritchard, K., and Marston, S. B. (1987) *J. Biol. Chem. 262*, 116.
9. Smith C. W., and Marston, S. B. (1985) *FEBS Lett. 184*, 115.
10. Sobue, K., Muramoto, Y., Fujita, M., and Kakiuchi, S. (1981) *Proc. Natl. Acad. Sci. U.S.A. 78*, 5652.
11. Babu, Y. S., Bugg, C. E., and Cook, W. J. (1988) *J. Mol. Biol. 204*, 191.
12. Herzberg, O., and James, M. N. G. (1988) *J. Mol. Biol. 203*, 761.
13. Satyshur, K. A., Rao, S. T., Pyzalska, D., Drendel, D., Drendel, M., Greaser, M., and Sundaralingam, M. (1988) *J. Biol. Chem. 263*, 1628.
14. Heidorn, D. B., and Trewhella, J. (1988) *Biochemistry 27*, 909.
15. Barbato, G., Ikura, M., Kay, L. E., Pastor, R. W., and Bax, A. (1992) *Biochemistry 31*, 5269.
16. Slupsky, C. M., and Sykes, B. D. (1995) *Biochemistry 34*, 15953.
17. Trewhella, J. (1994) in *Structural Biology: The State of the Art* (Sarma, R. H., and Sarma, M. H., Eds.) pp 43−57, Academic Press, New York.
18. Crivici, A., and Ikura, M. (1995) *Annu. Rev. Biophys. Biomol. Struct. 24*, 85.
19. James, P., Vorherr, T., and Carafoli, E. (1995) *Trends Biochem. Sci. 20*, 38.
20. Ikura, M. (1996) *Trends Biol. Sci. 21*, 14.
21. Heidorn, D. B., Seeger, P. A., Rokop, S. E., Blumenthal, D. K., Means, A. R., Crespi, H., and Trewhella, J. (1989) *Biochemistry 28*, 6757.
22. Ikura, M., Clore, G. M., Gronenborn, A. M., Zhu, G., Klee, C. B., and Bax, A. (1992) *Science 256*, 632.
23. Meador, W. E., Means, A. R., and Quiocho, F. A. (1992) *Science 257*, 1251.
24. Meador, W. E., Means, A. R., and Quiocho, F. A. (1993) *Science 262*, 1718.
25. Krueger, J. K., Olah, G. A., Rokop, S. E., Zhi, G., Stull, J. T., and Trewhella, J. (1997) *Biochemistry 36*, 6017.
26. Krueger, J. K., Zhi, G., Stull, J. T., and Trewhella, J. (1998b) *Biochemistry 37*, 13997.
27. Trewhella, J., Blumenthal, D. K., Rokop, S. E., and Seeger, P. A. (1990) *Biochemistry 29*, 9316.
28. Dasgupta, M., Honeycutt, T., and Blumenthal D. K. (1989) *J. Biol. Chem. 264*, 17156.
29. Olah, G. A., and Trewhella, J. (1994) *Biochemistry 33*, 12800.
30. Zhan, Q., Wong, S. S., and Wang, C.-L. A. (1991) *J. Biol. Chem. 266*, 21810.
31. Mezgueldi, M., Derancourt, J., Callas, B., Kassab, R., and Fattoum, A. (1994) *J. Biol. Chem. 269*, 12824.
32. Marston, S. B., Fraser, I. D. C., Huber, P. A. J., Pritchard, K., Gusev, N. B., and Torok, K. (1994) *J. Biol. Chem. 269*, 8134.
33. Zhuang, S., Wang, E., and Wang, C.-L. A. (1995) *J. Biol. Chem. 270*, 19964.
34. Mabuchi, Y., Wang, C.-L. A., and Grabarek, Z. (1995) *Biophys. J. 68*, A359.
35. Wang, E., Zhuang, S., Kordowska, J., Grabarek, Z., and Wang, C. L.-A. (1997) *Biochemistry 36*, 15026.
36. Krigbaum, W. R., and Kugler, F. R. (1970) *Biochemistry 9*, 1216.
37. Krueger, J. K., Bishop, N. A., Blumenthal, D. K., Zhi, G., Beckingham, K., Stull, J. T., and Trewhella, J. (1998a) *Biochemistry 37*, 17810.
38. Moore, P. B. (1980) *J. Appl. Crystallogr. 13*, 168.
39. Svergun, D. I., Smemnyuk, A. V., and Feigin, L. A. (1988) *Acta Crystallogr. A44*, 244.
40. Guinier, A. (1939) *Ann. Phys. (Paris) 12*, 161.
41. Wakatsuki, S., Hodgson, K. O., Eliezer, D., and Rice, M. (1992) *Rev. Sci. Instrum. 63*, 1736.
42. Gallagher, S. C., Callaghan, A. J., Zhao, J., Dalton, H., and Trewhella, J. (1999) *Biochemistry 38*, 6752.
43. Hammouda, B., Barker, J. G., and Krueger, S. (1996) *Small-angle Neutron Scattering Manuals*, NIST, Gaithersberg, MD.
44. Olah, G. A., Rokop, S. E., Wang, C.-L. A., Blechner, S. L., and Trewhella, J. (1994) *Biochemistry 33*, 8233.
45. Trewhella, J., Liddle, W. K., Heidorn, D. B., and Strynadka, N. (1989) *Biochemistry 28*, 1294.
46. Svergun, D. I., Volkov, V. V., Kozin, M. B., and Stuhrmann, H. B. (1996) *Acta Crystallogr. A52*, 419.

47. Svergun, D. I., Volkov, V. V., Kozin, M. B., Stuhrmann, H. B., Barberato, C., and Koch, M. H. J. (1997) *J. Appl. Crystallogr. 30*, 798.
48. Svergun, D., Barberato, C., and Koch, M. H. J. (1995) *J. Appl. Crystallogr. 28*, 768.
49. Zhao, J., Hoye, E., Boylan, S., Walsh, D. A., and Trewhella, J. (1998) *J. Biol. Chem. 273*, 30448.
50. Stuhrmann, H. B. (1987) in *Methods of Experimental Physics*, pp 367−403, Academic Press, Inc., New York.
51. Byler, M. D., and Susi, H. (1986) *Biopolymers 25*, 469.
52. VanStokkum, I. H. M., Linsdell, H., Hadden, J. M., Haris, O. I., Chapman, D., and Blomendal, M. (1995) *Biochemistry 34*, 10508.
53. Zhou, N., Yuan, T., Mak, A. S., and Vogel, H. J. (1997) *Biochemistry 36*, 2817.
54. Zhang, M., and Vogel, H. J. (1994) *Biochemistry 33*, 1163.
55. Zhang, M., Fabian, H., Mantsch, H. H., and Vogel, H. J. (1994) *Biochemistry 33*, 10883.
56. Blechner, S. L., Olah, G. A., Strynadka, N. C. J., Hodges, R. S., and Trewhella, J. (1992) *Biochemistry 31*, 11326.
57. Stone, D. B., Timmins, P. A., Schneider, D. K., Krylova, I., Ramos, C. H. I., Reinach, F. C., and Mendelson, R. A. (1998) *J. Mol. Biol. 281*, 689.

BI992638X